Molecular Biomechanics of the TAS2R46 Bitter Taste Receptor through Network-based Investigation

Marco Cannariato[a], Riccardo Fanunza[a], Eric A. Zizzi[a], Marcello Miceli[a], Giacomo Di Benedetto[b], Marco A. Deriu[a] and Lorenzo Pallante[a,*]

[a]Polito[BIO]Med Lab, Department of Mechanical and Aerospace Engineering, Politecnico di Torino, 10129, Turin, Italy

[b]7HC s.r.l., 00198, Rome, Italy

*Corresponding author: Corso Duca degli Abruzzi 24, 10129, Turin, Italy. E-mail: lorenzo.pallante@polito.it (LP)

Highlights

- The dynamics of active and inactive TAS2R46 were studied through network analysis.
- Ligand binding to TAS2R46 increases intra-protein correlations.
- TM3 and TM6 helices mediate the structural signalling in active TAS2R46.
- Rotation of Y241 residue is pivotal for the structural signalling in active TAS2R46.

Abstract

The intricate relationship between structural characteristics and the resultant signal-processing events is fundamental in comprehending the functions and mechanisms inherent in biomolecular systems, specifically proteins. G protein-coupled receptors (GPCRs) constitute one of the most prevalent protein families within the human organism, engaging in a wide spectrum of vital functions. The TAS2Rs, a subfamily of G protein-coupled receptors (GPCRs), play a primary role in recognizing bitter molecules and initiate a cascade of events leading to the perception of a bitter taste. This gustatory sensation is associated with protecting the organism against the ingestion of spoiled or poisonous food. Interestingly, TAS2Rs function is not limited to taste evaluation, but it is associated with many diseases as they are expressed in several extra-oral tissues. Since the precise mechanism of TAS2R activation is poorly understood, this work aims to characterize the mechanisms underlying the signal transduction on the recently experimentally solved hTAS2R46 bitter taste receptor using molecular dynamics simulations coupled with network-based analysis. The results show that receptor activation is associated with a more correlated dynamics of the receptor and the formation of an interaction between two helices which mainly convey the signal transferring from the extracellular to the intracellular region. By highlighting TAS2R46 activation hallmarks and proposing a methodology for the characterization of bitter taste receptor activation, this study lays the foundation for a general understanding of the functioning mechanisms of this fascinating class of receptors.

Keywords: Bitter; Taste Receptor; Molecular Dynamics; Network Analysis.

1 Introduction

The sense of taste, also known as gustation, is crucial for mammals in evaluating the taste and composition of foods (Roper, 2017). Bitter, along with sweet, sour, salty, and umami, is one of the five basic taste modalities and allows to distinguish toxic molecules, providing the last checkpoint before the ingestion of potentially harmful substances. Bitter taste arises from the interaction of organic bitter molecules with type 2 taste receptors (TAS2Rs), which is a subfamily of G protein-coupled receptors (GPCRs) (Chandrashekar et al., 2000). These taste receptors are mainly expressed

on the functional gustatory transduction units, i.e. the taste buds of the tongue, which are contained in gustatory papillae. Bitter compounds, binding to TAS2Rs, induce receptor conformational changes and initiate a downstream cascade of events inside the cell typical of GPCR signalling pathways, which ultimately leads to bitter taste perception. It is worth noticing that TAS2Rs are not only located in the taste buds of the tongue, but also several extra-oral tissues express them, such as heart, skeletal and smooth muscle, upper and lower airways, gut, adipose tissue, brain, and immune cells (Behrens and Meyerhof, 2013; Lee et al., 2019). Therefore, their function is not limited to taste evaluation, but it is associated with many diseases, such as asthma or diabetes (Dotson et al., 2008; Liggett, 2014; Pan et al., 2017). Therefore, extra-oral TAS2Rs could also represent a promising target for pharmacological intervention for specific diseases or health conditions. In this scenario, the understanding of the molecular mechanisms driving TAS2R functions is not limited to the taste perception field but can also improve our knowledge for pathologies and relative treatments.

From a structural point of view, TAS2Rs include a short extracellular N-terminus domain, an intracellular C-terminus domain, and seven transmembrane α-helixes (7TMs), which are connected by three extracellular loops (ECLs) and three intracellular loops (ICLs) (Zhang et al., 2017). These receptors present a unique binding pocket which is in the EC part of the 7TMs bundle, involving the extracellular region of TMs II, III, V, VI, VII (Pallante et al., 2021). The secondary structure of these receptors is composed mainly of alpha-helix associated with the transmembrane bundle (about 70-75%), whereas there are about 20% of bend, coil, and turn and, in some cases, a minor part of beta-sheets (1-2%), composing the EC and IC domains. Despite being promising pharmacological targets for various diseases, no experimental structure of bitter taste receptors has been determined until recently, when cryo-electron microscopy structures of human TAS2R46 in both active form and inactive states were revealed (Xu et al., 2022). In particular, in the active form, TAS2R46 is bound to strychnine, a toxic bitter alkaloid known to be one of the main agonists that activate the TAS2R46-G-protein signalling pathway (Brockhoff et al., 2007). From the comparison of the experimental active and inactive structures, the typical conformational changes related to class A GPCRs, in which TAS2Rs were usually inserted, were not observed, thus leading to the classification of TAS2Rs as class T GPCRs. Furthermore, the only large conformational change detected was the different localization of the ECL2, which occupied the orthosteric binding pocket in the inactive state. Finally, a rotation of the Y241 side chain toward the centre of the 7TMs bundle was observed in the active state.

Whereas the recent resolution of TAS2R46 shed new light on the study of the bitter taste receptors activation process, the conformational features and the molecular mechanisms underlying the signal transferring from the EC to the IC environment are still poorly understood. Computational techniques, including Molecular Dynamics (MD) and Machine Learning, are rapidly becoming paramount techniques to highlight the key molecular features linked to the recognition of small molecules by taste receptors and identify subsequent molecular events and activation mechanisms (Malavolta et al., 2022; Pallante et al., 2021; Soncini et al., 2007). Moreover, the analysis of MD simulations through graph-based approaches is becoming an elective method to study the intra-protein structural communication and crucial residues for protein functions, also in the case of GPCRs (Fanelli et al., 2016; Melo et al., 2020). Using MD simulations coupled with network-based techniques, the present study aims to characterize the active/inactive conformational states of the human TAS2R46 bitter taste receptor and investigate the molecular mechanisms at the basis of the transfer of information between the EC and IC regions. We simulated different receptor conditions to pinpoint major differences between the transfer of vibrational information in the active and inactive receptor states. Although the findings of this study are in good agreement with earlier research on comparable systems, they also provide valuable novel insights into the different dynamical properties of the active and inactive TAS2R46 states. Moreover, possible pathways involved in the signal transferring from the orthosteric binding site to the G-protein-coupled regions were highlighted. Therefore, this work

represents a step forward in the overall understanding of the molecular features underlying the activation mechanisms of the TAS2R46 bitter taste receptor.

2 Materials and Methods

2.1 System setup

The molecular structures of human TAS2R46 were retrieved from the RCSB Protein Data Bank, using the PDB codes 7XP6 and 7XP4 for strychnine-bound and Apo states, respectively (Xu et al., 2022). The uninterested entities were removed from the PDB files and only the receptor chain and eventually the ligand were preserved. The missing residues (157-172) of the experimental strychnine-bound TAS2R46 structure were modelled using the corresponding model from the AlphaFold Protein Structure Database (P59540 entry) (Jumper et al., 2021) after root-mean-square fitting on the alpha carbons of the experimental structure. The structure of strychnine was refined using MOE ("Molecular Operating Environment (MOE), 2022.02 Chemical Computing Group ULC, 1010 Sherbooke St. West, Suite #910, Montreal, QC, Canada, H3A 2R7, 2023.," 2022), assigning the correct protonation at neutral pH and salt concentration of 0.15 M. Therefore, two structures were obtained: (i) the receptor in its active state bound to strychnine (Holo) and (ii) the inactive receptor in absence of the ligand (Apo). A third structure, which will be referred to as Trans, was then defined by removing strychnine from the binding pocket of the Holo state.

For each of the three structures, the protein-membrane complex has been built using CHARMM-GUI (Feng et al., 2023) as follows. The homogeneous bilayer membrane was composed of phosphatidylcholine (POPC, 16:0/18:1 acyl chains), as reported in previous literature (Hénin et al., 2006; Zou et al., 2019). The system has been inserted in a rectangular box with dimensions of 8x8x11 nm. This choice allowed us to reach a good compromise between acceptable computational cost and the need to ensure the minimum image convention. Then, the system was solvated by using the TIP3P water model before adding an appropriate number of Na^+ and Cl^- ions to reach a physiological salt concentration of 0.15 M and neutralize the overall system charge. The AMBER19SB force field (Lee et al., 2020; Tian et al., 2020) was used to describe the protein, ions, and water, the Lipid-21 forcefield (Dickson et al., 2022) was used for lipids, and the General Amber Force Field (GAFF2) forcefield (Wang et al., 2004) to obtain the topology for strychnine. System preparation and topology definition were performed directly in CHARMM-GUI as done in previous literature (Muscat et al., 2020; Pallante et al., 2020; Pallante Lorenzo et al., 2023; Sztandera et al., 2021; Zizzi et al., 2022). The protein-membrane complexes in the Holo, Trans, and Apo states are shown in Figure 1.

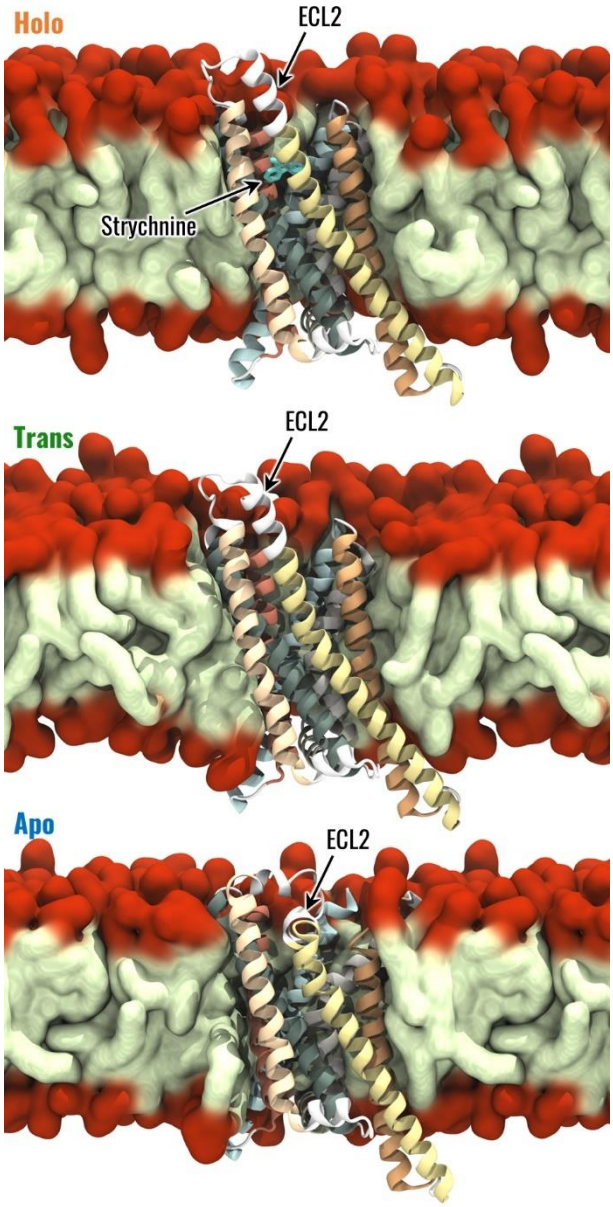

Figure 1. Visual representation of the Holo, Trans and Apo systems. The 7 TMs of TAS2R46 are highlighted with different colours, the hydrophobic tails and hydrophilic head of POPC are coloured in light green and red, respectively.

2.2 Molecular Dynamics Simulation

MD simulations were performed using the simulation engine GROMACS 2022 (Bauer et al., 2023) starting from the models described above. For each system, the same simulation protocol was followed as detailed below. First, energy minimization was performed through the steepest descent method for 5000 steps. Then, three replicas were performed following the CHARMM-GUI protocol of equilibration before a production phase of 500 ns long. In detail, six equilibration steps were performed gradually reducing the position restraints on the lipids and protein-heavy atoms (from 1000 to 0 $kJmol^{-1}nm^{-1}$ for lipids, from 4000 to 50 $kJmol^{-1}nm^{-1}$ for the protein backbone and from 2000 to 0 $kJmol^{-1}nm^{-1}$ for protein side-chain heavy atoms). The equilibration phase started with two NVT simulations, performed for 125 ps with a timestep of 1 fs. Then, four NPT equilibration steps were performed, the first one for 125 ps with a timestep of 1 fs, the remaining three for 500 ps with a timestep of 2 fs. The total time of equilibration of each replica was 1.875 ns. The NVT simulations were performed at a reference temperature of T=303,15 K (τ = 1 ps), which is above the phase-transition temperature for POPC, using the Berendsen thermostat (Berendsen et al., 1984), while NPT simulations were carried out at 1.0 bar using the Berendsen barostat with semi-isotropic coupling

(τ = 5 ps). Finally, the unrestrained production phase was carried out in the NPT ensemble with a Nose-Hoover thermostat and Parrinello-Rahman barostat for 500 ns. The leapfrog integrator was used, using a time step of 2 fs. The PME algorithm was used for electrostatic interactions with a cut-off of 0.9 nm. A reciprocal grid of 72 x 72 x 96 cells was used with 4th-order B-spline interpolation. A single cut-off of 0.9 nm was used for Van der Waals interactions. LINCS (LINear Constraint Solver) algorithm for h-bonds (Hess et al., 1997) was applied in each simulation step. Three simulation replicas were performed for each investigated system to increase the statistics of the data and ensure the repeatability of the results. Therefore, a total of 4.5 µs of simulation during the unrestrained simulation phase were performed.

2.3 Analysis

2.3.1 Conformational analysis

The structural stability throughout the MD simulations for each investigated state (Holo, Trans, Apo) was evaluated by considering the root-mean-squared deviation (RMSD) from the initial configuration of backbone atoms' positions during the trajectory. To further assess the structural stability of the identified equilibrium, a cluster analysis with the linkage algorithm of the concatenated last 400 ns of each replica was employed, using the RMSD between backbone atoms as metric and 0.15 nm as the cutoff. Moreover, the secondary structure probability for each protein residue was evaluated by considering the concatenated last 400 ns of each replica (Janaszewska et al., 2018). The root-mean-squared fluctuation (RMSF) of alpha carbons was computed in the last 400 ns of each replica, allowing the evaluation of the fluctuations of each residue during the simulation time. Once the structural stability was assessed, the equilibrium trajectories (last 400 ns of simulation) were concatenated obtaining a single 1.2 µs trajectory for each system under investigation. Then, the following analysis was performed considering a sampling time of 50 ps, unless otherwise specified.

The Protein-Ligand Interaction Profiler (PLIP) (Salentin et al., 2015) tool was used to evaluate the specific interactions between strychnine and TAS2R46, underlining the most important residues involved in strychnine binding and the types of interactions established (i.e. hydrogen bonds, hydrophobic interactions, salt bridges, etc.). In detail, the probability of a specific interaction between the receptor and strychnine has been evaluated by considering the interactions on each frame and then averaging the number of occurrences of the interactions on the total number of frames, as done previously (Miceli et al., 2022).

The binding pocket volume was evaluated using the Epock tool (Laurent et al., 2015). The maximum englobing region (MER), i.e., the region of space delimiting the binding pocket, was defined as a sphere of radius 1.3 nm located at the centre of mass of strychnine, considering the starting configuration of Holo replicas. Before the binding pocket volume evaluation, the concatenated trajectories were RMS fitted on the configuration used to define the MER. Moreover, in the analysis, the residues 153 to 176 and, in the Holo system, strychnine were not considered to allow a better comparison between the three systems under study.

Then, the conformation of Y241, whose side chain is characterized by a different position in the experimental structures of human TAS2R46, was described by the angle θ, defined as the angle between the centre of mass of Y241 aromatic ring, the alpha carbon of Y241, and the alpha carbon of Y271.

The calculation of RMSD, RMSF, and cluster analysis was performed using GROMACS, whereas the secondary structure was evaluated through the STRIDE (Heinig and Frishman, 2004) software package. Conformational analysis was performed through custom-made scripts in Python using the MDAnalysis module. All plots were generated using the Matplotlib (Hunter, 2007) and Seaborn (Waskom, 2021) libraries, whereas the three-dimensional representations of receptor structures were rendered in Visual Molecular Dynamics (VMD) software (Humphrey et al., 1996).

2.3.2 Generalized correlation analysis

A correlation analysis was also employed to identify the regions of the receptor more correlated with each other in the Holo, Trans, and Apo states. In particular, the generalized correlation coefficient (r_{MI}) was computed as it takes into account linear and non-linear contributions to correlations (Lange and Grubmüller, 2005). This analysis was performed since correlated motions are essential for the biomolecular function of several systems, such as orthosteric and structural signal transduction in GPCRs (Scheer and Cotecchia, 1997).

The generalized correlation coefficient between residues *i* and *j* has been computed as:

$$r_{MI}[i,j] = (1 - e^{-\frac{2}{3}I[i,j]})^{\frac{1}{2}}$$

where $I[i,j]$ is the mutual information between the positions of residues *i* and *j*, where the position of one residue was defined as the position of its alpha carbon. The mutual information has been computed using the density estimator described by Kraskov et al. (Kraskov et al., 2004) with neighbour parameter *k* of 6 as done in previous literature (Lange and Grubmüller, 2005; Melo et al., 2020):

$$I[i,j] = \psi(k) - \frac{1}{k} - \langle \psi(n_i) + \psi(n_j) \rangle + \psi(N)$$

where *N* is the total number of simulation frames, $\psi(x)$ is the digamma function, n_i is the number of frames in which residue *i* is close to the one in the reference, and ⟨ ⟩ stands for the average by varying the reference frame over the trajectory. For the generalized correlation coefficient calculation, a trajectory sampling time of 1 ns was considered to avoid considering correlated frames in the analysis as done in previous literature (Cannariato et al., in press; Manrique et al., 2023).

2.3.3 Dynamic Network Analysis

To investigate structural communication within the TAS2R46 receptor, the MD simulations were analyzed through the Dynamical Network Analysis approach, using the dynetan library (Melo et al., 2020). This specific network analysis was selected as it is based on the generalized correlation coefficient, thus considering nonlinear contributions to amino acid dynamical correlations. In detail, in the Dynamical Network Analysis, each protein residue was represented by a node located in its alpha carbon and strychnine was modelled through a single node in the closest atom to its centre of mass. Nodes were linked with edges if the frequency of contacts between the corresponding residues was greater or equal to 0.75, considering two residues to be in contact at a simulation frame if the shortest distance between their heavy atoms is lower than 0.45 nm. The edges of the obtained graph were weighted using the generalized correlation coefficient (Lange and Grubmüller, 2005), computed using a sampling time of 1 ns (Manrique et al., 2023). The network was characterized in terms of betweenness centrality and eigenvector centrality. The betweenness centrality of an edge or node is described as the fraction of the shortest paths in which the considered edge or node is involved and highlights the importance of edges and nodes for the connection of distant parts of the network. In this study, the shortest path between two nodes was defined as the path that maximizes the sum of correlations between the nodes involved in the path. The betweenness centrality is computed as:

$$b_i = \frac{1}{C} \sum_{s,t \in V} \frac{\sigma(s,t|i)}{\sigma(s,t)}$$

where $\sigma(s,t)$ is the number of shortest paths between nodes *s* and *t*, $\sigma(s,t|e)$ is the number of such paths passing through node *e*, *V* is the ensemble of graph nodes, and *C* is a normalization factor to

allow the comparison of networks with different numbers of nodes. In particular, for a graph of *n* nodes, is equal to

$$\frac{2}{(n-1)(n-2)} \text{ or } \frac{2}{n(n-1)}$$

for node and edge betweennesses, respectively.

The eigenvector centrality of a network measures the influence of a node in a graph considering the topology of the graph itself, such that the centrality of a node depends on the centrality of its neighbours. Therefore, if a node has many connections with nodes of small influence, it will also have a small centrality in the network. On the other hand, if a node has few connections with nodes very influential in the network, it might have high centrality because of its indirect influence within the graph. Mathematically, the eigenvector centrality of node *i* is the *i-th* entry of the eigenvector (x) of the adjacency matrix weighted on the correlation between the nodes (A):

$$Ax = \lambda x$$

3 Results

From the visual inspection of the RMSD plots, it was concluded that the structural stability of the systems on each replica was reached after the first 100 ns (Figure S1). The structural stability was confirmed by the cluster analysis of the concatenated trajectories (last 400 ns of each replica), which showed only one cluster per system. Moreover, the stability of the receptor structure was analyzed in terms of secondary structure probability. This analysis highlighted that the TMs maintained their structure across the simulations without any remarkable alteration of their secondary structure regardless of the receptor's configuration state (Figure S2). Once the structural stability was confirmed, the Holo, Trans, and Apo systems were characterized as follows. First, we analyzed the difference between the systems in terms of the conformation of the receptor. Subsequently, we examined the dynamic correlations within the structure of the receptor to emphasize distinctions and similarities in the dynamic properties contingent on the TAS2R46 state. Finally, we considered how the difference in conformation and correlation result in different patterns of structural communication inside the receptor through the dynamic network analysis.

3.1 Conformational features of TAS2R46 activation

This paragraph describes the conformational analysis conducted to identify remarkable differences among the three analyzed states - Holo, Trans, and Apo. The objective of these analyses is to identify specific structural characteristics associated with the active and inactive states of TAS2R46.

The Holo, Trans, and Apo states were initially characterized in terms of RMSF, which was computed to evaluate the flexibility of the different receptor regions. As expected, the most flexible regions of TAS2R46 were the unstructured ones and some differences have been observed between the three receptor states for ICL3 and ECL3 (Figure S3). The Trans state is characterized by higher fluctuations in the ECL3, but the flexibility of the ICL3 in this state is the same as the Holo state. Interestingly, the ICL3 region is more stable and less flexible in the Apo state compared to the other two. On the other side, the ECL2 displays similar fluctuations in the three systems, although it is characterized by a different conformation in the Apo state compared to the Holo and Trans states (Figure 1). Finally, the interaction between strychnine and the receptor was analyzed in terms of type and stability using PLIP. This analysis revealed three main interactions with a probability greater than 0.5, namely two hydrophobic interactions with residues Y85 and W88 and a salt bridge interaction with E265 (Figure S4). This confirms that the main interactions detected in the experimental structure are conserved and involve the TM3 and TM7, highlighting the stability of the ligand inside the receptor's binding pocket during the simulations.

Since a rotation of the Y241 side chain from pointing outward the 7TMs bundle to pointing into the core of the receptor has been previously reported for TAS2R46 (Xu et al., 2022), the conformation of the Y241 side chain has been defined in terms of the angle θ, shown in Figure 2A, defined as the angle between the centre of mass of Y241 aromatic ring, the alpha carbon of Y241, and the alpha carbon of Y271. According to its definition, higher values of θ can be related to conformations in which Y241 points towards the centre of the receptor. The results show that the conformations of Y241 during the MD simulations remained in line with the experimental observations, with higher θ values for the Holo state. Interestingly, the removal of Strychine seemed to destabilize Y241 conformation, whose distribution of θ in the Trans state was located between the ones of the Holo and Apo states. However, the different conformations of Y241 are not related to outward movements of the IC region of TM6, which is one of the hallmarks of the class A GPCRs activation process (Zhou et al., 2019): the distance between the IC areas of TM3 and TM6 does not show remarkable differences between the three states despite the different values of θ (see also Figure S5), strengthening the previously observed different behaviour compared to class A GPCRs (Xu et al., 2022).

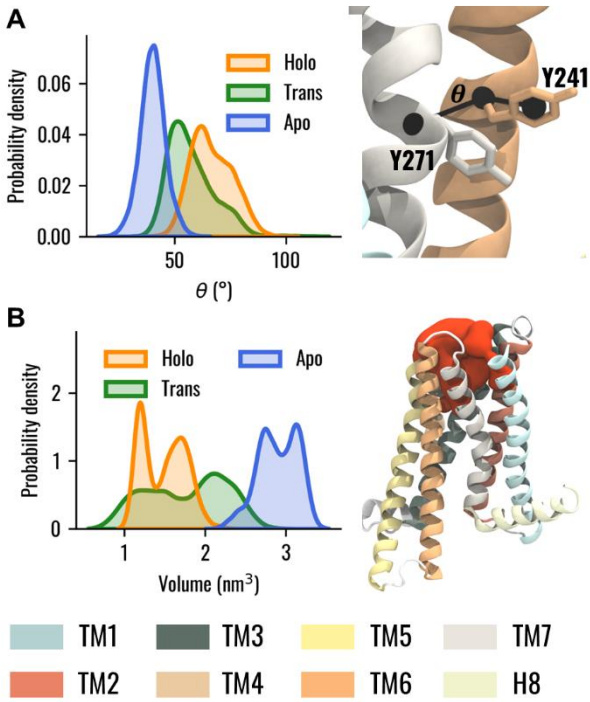

Figure 2. Conformational analysis of TAS2R46 in the three investigated states. (**A**) Probability distribution of the θ angle for Holo, Trans, and Apo states (left) and visual representation of angle θ definition (right). (**B**) Probability distribution of the binding pocket volume for the Holo, Trans, and Apo states (left) and visual representation of the binding pocket volume, coloured in red, for one selected frame of the Apo system (right).

Then, the volume of the TAS2R46 binding pocket was evaluated in the three systems. It is worth mentioning that, in this analysis, the ECL2 was not considered to prevent any alterations in the estimation, as it is located inside the investigated pocket in the Apo state. The results showed that the volume of the orthosteric pocket is higher in the absence of strychnine (Figure 2B). Interestingly, the Trans state displayed an intermediate behaviour as it is characterized by a distribution of the volume located between the ones of Apo and Holo states.

3.2 Receptor active state is related to increased dynamical correlation

In this section, we assessed intra-structure correlations and examined how they were altered by the presence or absence of strychnine to identify major differences. The correlation between the different receptor regions in the three states was analyzed using the generalized correlation coefficients as

described in the Material and Methods section. We evaluated the correlation between residues for the Holo, Trans, and Apo states, which showed remarkable differences in their dynamic behaviour. In the Holo system, high correlations were observed between the EC region of the receptor, whereas the IC regions of TM5 and especially TM6 were less correlated with the rest of the 7TM bundle (Figure 3A). Interestingly, the ICL3 displayed higher correlations than the neighbouring regions of TM5 and TM6, especially with the ECL1. Our results also showed that the removal of strychnine from the orthosteric binding pocket induced a remarkable and general loss of dynamic correlation (more bluish areas) within the 7TM bundle (Figure 3B). High correlations for the Trans state were observed only for the EC regions of TM1, TM6, and TM7, the ECL2, and, less markedly, the ECL1. On the other hand, the regions showing the lowest correlation with the 7TM bundle were the IC regions of TM3, TM6, and TM7. Finally, in the Apo state, the results highlighted remarkable correlations of the ECL2 with the EC regions of the receptor, while lower values could be observed for the IC regions (Figure 3C). To easily compare the receptor states, we also calculated the differences of the generalized correlation coefficient between the Trans and Holo states, i.e. Δr_{MI}(Trans, Holo) = r_{MI}(Trans) - r_{MI}(Holo), and between the Apo and Holo states, i.e. Δr_{MI}(Apo, Holo) = r_{MI}(Apo) - r_{MI}(Holo) (Figure 3D). Comparing the observed correlations for the three states, it was observed that, in general, the receptor evolved dynamically in a more correlated way in the presence of strychnine, whereas its absence was associated with the decorrelation of the IC regions. Moreover, it is worth noticing that the Trans state overall demonstrated lower structural correlation values compared to the other two. Furthermore, Figure 3D highlighted that the ICL3 and the IC portion of TM3 are less correlated with the rest of the 7TM bundle in Trans and Apo states than in the Holo system. Interestingly, for both Trans and Apo systems, the IC portion of TM6 is more correlated with the rest of the receptor compared to the Holo state. Therefore, the Apo and Trans systems behaved in the same way if compared to the Holo state.

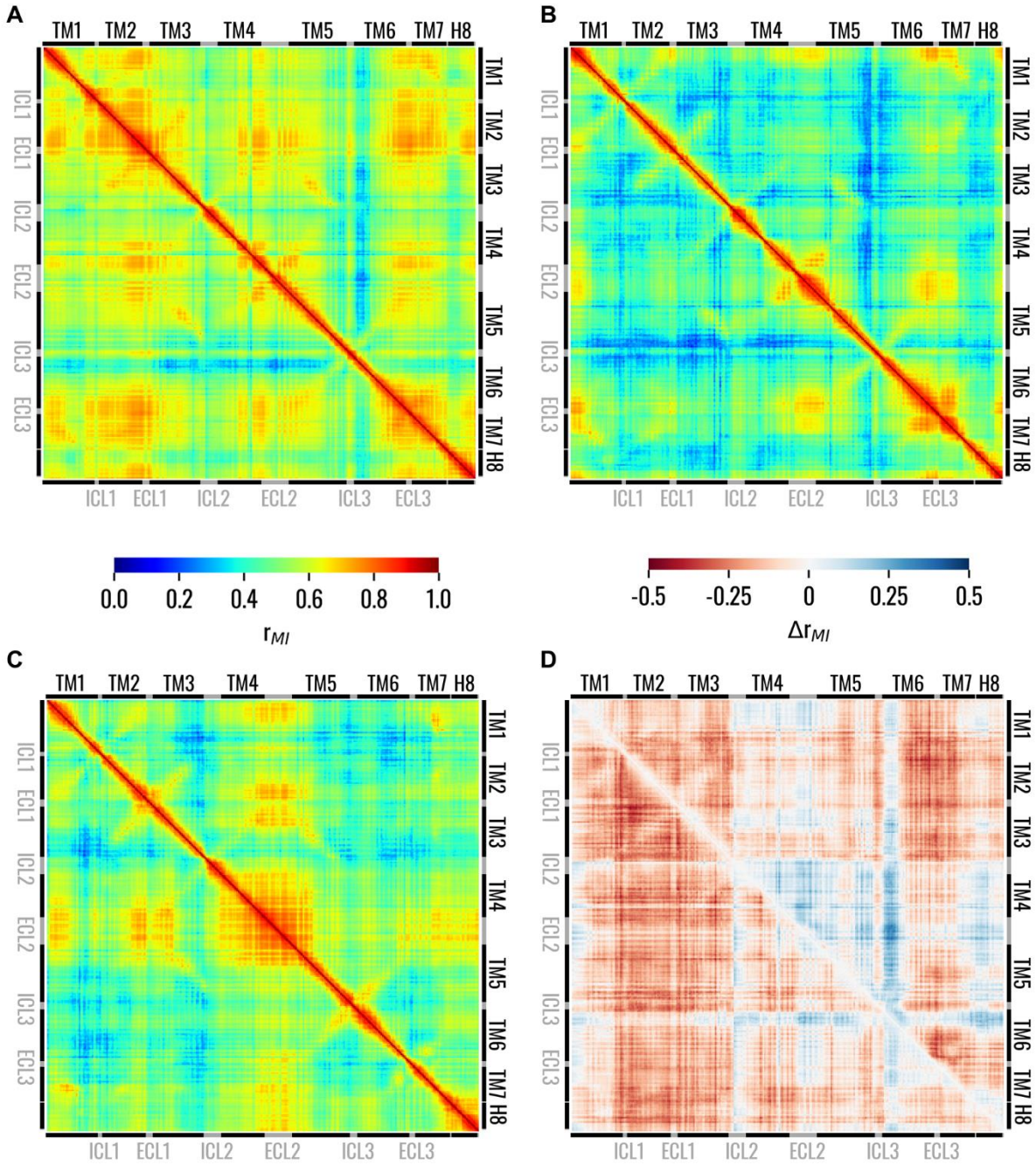

Figure 3: Matrices showing the generalized correlation coefficient between the residues of TAS2R46 in the (A) Holo, (B) Trans, and (C) Apo states. In panel (D), the differences of the generalized correlation coefficients are shown: Δr_{MI}(Trans, Holo) = r_{MI}(Trans) - r_{MI}(Holo) in the lower triangle and Δr_{MI}(Apo, Holo) = r_{MI}(Apo) - r_{MI}(Holo) in the upper triangle. Matrices on panels from A to C are coloured according to the left colorbar, while the matrix on panel D is colored according to the right colorbar.

3.3 Holo structural signalling is mediated by TM3-TM6 connection

The dynamic networks of Holo, Trans, and Apo systems were initially analyzed by extracting information regarding node and edge centralities from the graph topology. Plotting the node and edge betweenness centrality versus the node and edge rank showed that both betweennesses had similar values in the three networks (Figure S6). The knees of these curves were identified, for each of the three systems and both node and edge betweennesses, and the lowest ones, belonging to the Holo state, were used as thresholds. Then, only nodes or edges with betweenness higher than the identified threshold were considered in the subsequent analysis. The distribution of node betweenness

centralities in the different helices of the receptor was first considered, with specific attention to the upper tails of the distributions and outliers, which highlight residues of particular importance in the information flow inside the receptor. From this analysis, it was observed that, for the Holo state, the TM3 and TM6 were characterized by tails extending toward higher centralities, while other isolated residues were more central in other helices like TM1. On the other hand, for the Trans and Apo states, residues belonging to the TM3 were in general higher than the TM6 ones ($p < 0.05$ with Wilcoxon-signed-rank test), especially in the case of the Trans system (Figure 4A). Moreover, it could be observed that the tail of the distribution for TM4 extends toward higher values for Holo and Trans states compared to the Apo state. Finally, while the Holo and Apo systems showed similar ranges for TM2 and TM5 distributions, in these regions the Trans system was characterized by tails reaching higher centralities. Given that the betweenness centrality of nodes measures how influential a node is in the flow of information inside the network, these results highlight that the flow of information in TAS2R46 is mainly conveyed by the TM3 in the absence of strychnine, while by both TM3 and TM6 in the presence of the ligand. Similar information can be obtained from the visual inspection of the networks if the edges betweenness centrality is highlighted (Figure S7).

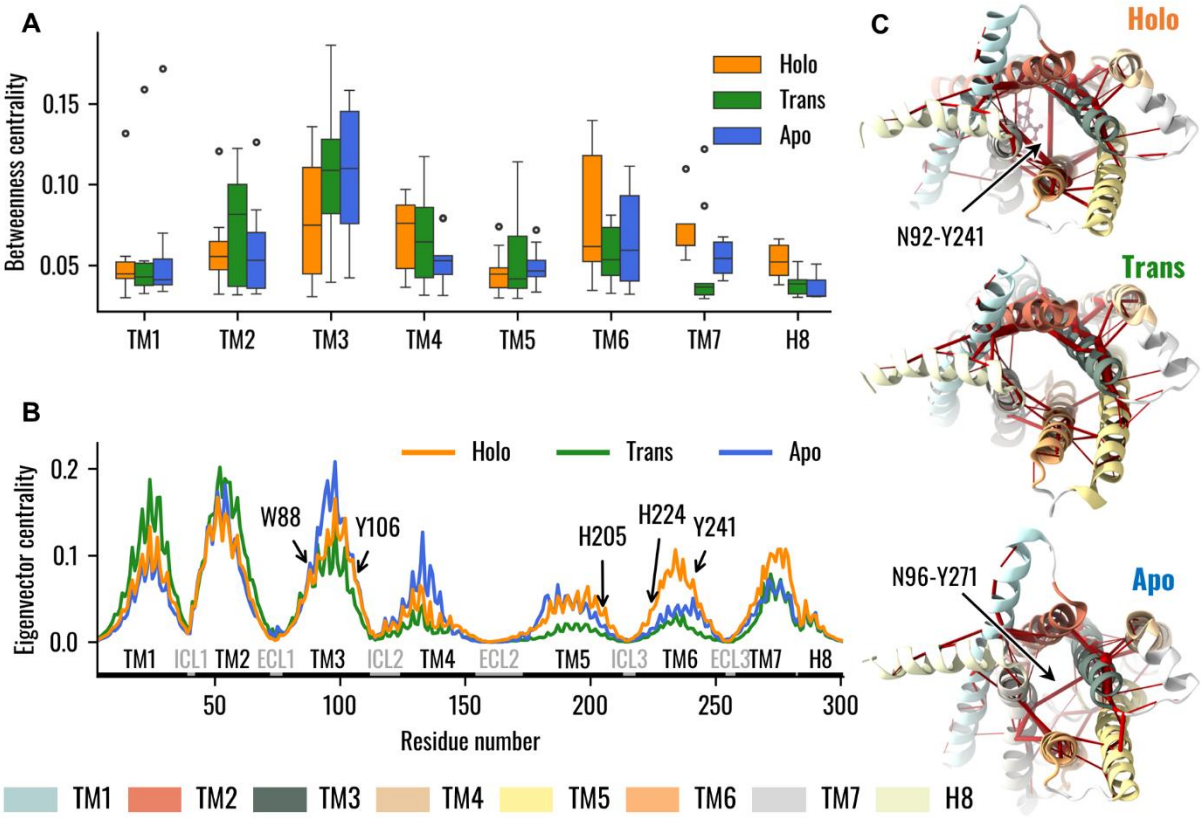

Figure 4. Dynamical Network Analysis of the Holo, Trans, and Apo systems. (**A**) Boxplots representing the distribution of node betweenness centrality, with nodes grouped into the respective TMs. Data emphasize that in the absence of the ligand TM3 assumed a primary role in information transfer, whereas in the presence of strychnine TM6 nodes also demonstrated high values of betweenness centrality. (**B**) Eigenvector centrality of TAS2R46 nodes. The TMs and loops are highlighted as well as residues pinpointed in previous experimental analysis. Results showed higher centrality of TM6 with strychnine, especially for H205, H224, and Y241, and decreased centralities in the Trans state. (**C**) Visual representation of the dynamic networks, where the receptor is viewed from the IC region. The edges of the network are red cylinders with a radius proportional to the betweenness centrality of the edge.

The influence of the single residues on the overall network was also analyzed in terms of eigenvector centrality. The results showed similar values for the EC and IC portions of the TM3 in the Apo and Holo systems, while the TM6 was characterized by remarkably higher centrality in the presence of strychnine (Figure 4B). In particular, while W88, involved in strychnine binding, and Y106, involved in G-protein interaction at the TM3 level (Xu et al., 2022), displayed similar centralities in Holo and

Apo states, H205, H224, and Y241 were more central in the presence of the ligand. Moreover, except for W88, all mentioned residues showed lower centralities in the Trans systems. This is particularly interesting as H205 and H224 are involved in G-protein interaction at the TM5 and TM6 levels, respectively (Xu et al., 2022). Moreover, as discussed before, Y241 has to have a pivotal role in TAS2R46 activation.

Finally, we focused on the difference, between the three systems under analysis, in terms of connections between TMs. Interestingly, the results showed that the main difference is relative to the TM3 (Figure S8): whereas in the presence of the ligand, there is a connection between TM3 and TM6 mediated by the interaction between N92 and Y241, in the inactive state TM3 is connected to TM7 through the N96-Y271 interaction, and in the Trans state there is no connection between TM3 and TM6 or TM7 (Figure 4C and see also Figure S8).

To investigate the effects of the highlighted changes in the dynamic network properties on the structural communication inside TAS2R46, we computed the optimal paths linking strychnine binding residues, in particular W88 and E265, to Y106 and H244, as in a previous study they were identified as G-protein binding residues (Xu et al., 2022). In line with the analysis of the network topology (Figure S8), in all systems the communication between W88 and Y106 is driven by the TM3 and the connection between E265 and H224 by the TM6. On the other hand, differences could be observed when considering the W88-H224 and E265-Y106 paths (Figure 5). In the presence of strychnine, both paths involve the edge between N92 and Y241, which creates a bridge between TM3 and TM6 through which the information between the EC and IC regions is conveyed. In the Apo state, instead, the path from W88 to H224 reaches the IC region of the receptor mainly through the TM3, then passes to the TM5, and finally to H224. Interestingly, the same path was observed in the Trans state, with the only difference being that the path reaches TM6 at H224 residue, instead of A227 as in the Apo state. On the other side, the connection between E265 and Y106 for the Apo system is mediated by the Y271-N96 interaction linking TM3 and TM7, whereas in the Trans system, the path is mediated by the TM2. Therefore, the change in the network topology is reflected in remarkable differences in the communication between the EC and IC regions.

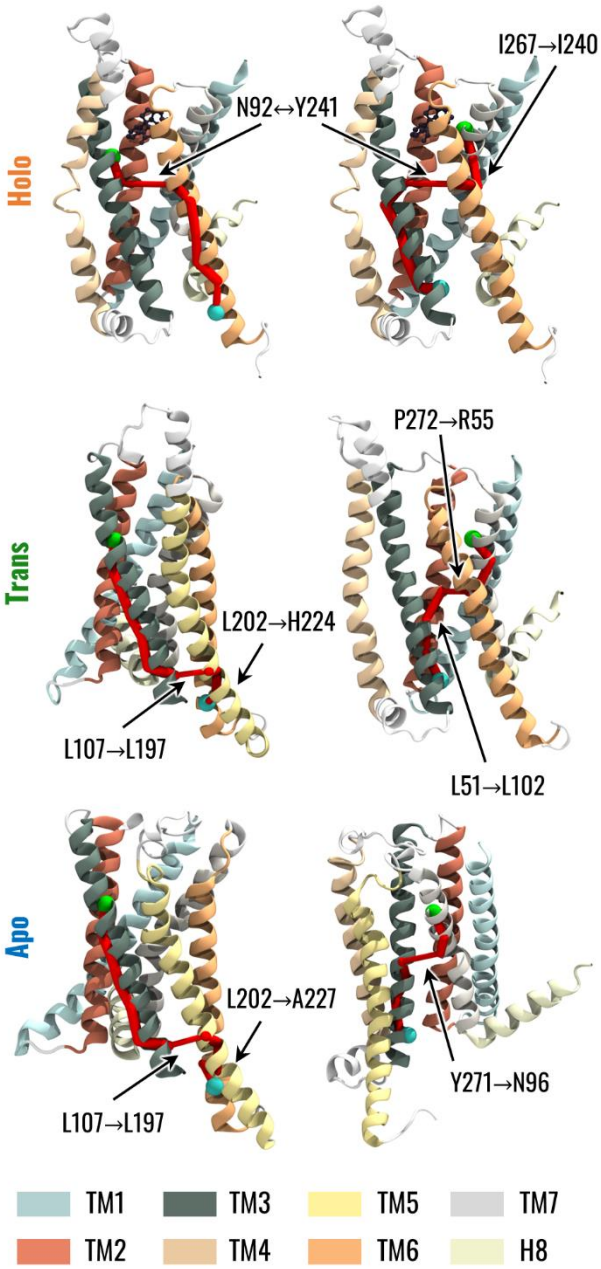

Figure 5. Visual representation of the optimal path connecting strychnine- and G protein-binding residues. The left column represents the communication path between W88 in TM3, highlighted as a green sphere, and H224 in TM6, represented as a cyan sphere. The right column represents the communication path between E265 in TM7, highlighted as a green sphere, and Y106 in TM3, represented as a cyan sphere. The edges in the paths are represented by cylinders whose radius is proportional to the generalized correlation coefficient between residues.

4 Discussion

TAS2Rs represent the basis of bitter taste perception, but at the same time there is increasing evidence that several extra-oral tissues express bitter taste receptors, and the activation of these extra-oral TAS2Rs leads to different signals and cellular responses that depend on the location and that, in general, are fundamental for metabolism and homeostasis (Dotson et al., 2008; Liggett, 2014; Pan et al., 2017). Extra-oral TAS2Rs are associated with several diseases, and they could represent a promising target for pharmacological intervention. However, the lack of experimental structures of TAS2Rs represented an important hurdle for understanding the mechanisms underlying bitter receptor activation. Nevertheless, the recent release of experimental structures of TAS2R46, in active (coupled with strychnine) and inactive (ligand-free) states, paves the way for the identification of

main events upon the TAS2R activation (Xu et al., 2022). Strychnine is of important interest as a ligand because it is experimentally known to target not only TAS2R46 (Brockhoff et al., 2010) but also other bitter taste receptors, such as TAS2R10 (Born et al., 2013), and even other proteins (Jensen et al., 2006). In this context, this work aims to contribute to the overall understanding of the molecular mechanisms related to the triggering of signalling pathways that lead to bitter taste perception. In particular, the case of TAS2R46 was considered and the key features of its activation process were explored, underlining the main differences between the active and inactive states. In detail, the conformational and dynamical features of the receptor in the presence and absence of strychnine were considered and then the dynamic network analysis was employed to investigate how such features could be related to the transfer of mechanical signals between the EC and IC regions of the receptor. Indeed, network analysis of protein dynamics represents a powerful technique for analyzing the structural communication in receptors such as the GPCRs (Fanelli et al., 2016; Melo et al., 2020; Sullivan et al., 2020).

Initially, conformational features typical of class A GPCRs or highlighted by previous experimental studies were considered. Regarding the interaction between strychnine and TAS2R46, the PLIP analysis on the MD simulation showed that the initial interactions with W88 and E265 remained stable, and at the same time pinpointed a stable hydrophobic interaction with Y85 (Figure S4). Moreover, our analysis confirmed previous evidence regarding the absence of class A GPCR conformational activation hallmarks, such as the outward movements of the IC region of TM6 (Figure S5) or the increase in the A^{100} index (Figure S9). These observations strengthen the recent new classification of TAS2Rs into the class T of GPCRs (Pándy-Szekeres et al., 2023), characterized by distinctive features different from class A (Di Pizio et al., 2016; Topin et al., 2021). Interestingly, as was observed for the class A GPCRs activation process (Dalton et al., 2015), in the TAS2R46 active state the volume of the orthosteric binding pocket is lower than the one in the inactive state. Moreover, the removal of strychnine from the Holo system was associated with an increase in the pocket volume (Figure 2B). Whereas the difference in the volume of Holo and Apo states could be related to the difference in ECL2 location (Figure 1), the increase observed for the Trans state was linked to side chain rearrangements as the ECL2 was located outside the binding pocket.

Among the side chain rearrangements, we focused on the rotation of Y241 observed in the experimental structure (Xu et al., 2022), which was proposed as the “toggle switch” feature of the activation process. The MD simulations confirm that the side chain of Y241, whose position was described through the angle θ, points towards the centre of the 7TM bundle in the presence of strychnine, forming an interaction with N92 in TM3, and towards the TM7 in the Apo states (Figure 2A). Interestingly, the removal of strychnine altered the conformation of Y241, which showed a tendency to rotate towards the TM7, placing the Trans state between the active and inactive conformation of TAS2R46.

Whereas the removal of strychnine induced a partial transition towards the inactive state of the receptor from a conformational point of view, the dynamic of TAS2R46 was remarkably influenced by such removal. This was highlighted by the analysis of the intra-receptor correlations, which showed higher overall correlation values for the Holo state, while both the Trans and the Apo states were characterized by lower correlations than the active state (Figure 3). In particular, in Trans and Apo states, reduced correlation for the IC region of TM3 and for the ICL3, which are important regions for G-protein binding, was observed. Therefore, the Apo and Trans systems were characterized by similar behaviour in terms of intra-receptor correlations if compared to the Holo state. The main difference between the Apo and Trans states could be linked to the different conformation of the ECL2. Whereas in the Apo state, where it is located inside the orthosteric binding site, the ECL2 is the main region whose motion is correlated with other regions in the receptor, in the Trans state this event was not observed, probably due to the ECL2 being outside the binding pocket. Therefore, the whole receptor seemed to evolve in time in a more decorrelated way. Furthermore, it

is noteworthy that perturbation caused by the removal of strychnine in the Trans state resulted in a globally less correlated state if compared to the Apo and Holo states.

The different conformational and dynamical features of the receptor in the three states were then related to different behaviours of the receptor in terms of structural communication. The analysis of the betweenness centrality pointed out the importance of TM3 in the transfer of information from the EC to the IC region of the receptor independently of its state. However, the TM6 was characterized by increased importance and influence inside the network in the presence of strychnine (Holo state) (Figure 4A,B). This information is particularly relevant as it highlights that high values of the centrality of TM6 in the presence of strychnine are related to its connection to TM3, which conveys the information flow mediated by Y241. In the Holo system, Y241 formed an edge with N92 in TM3 (Figure 4C) thanks to the different conformation of its side chain, forming a bridge that connects the main TMs involved in the structural communication between the EC and IC regions (Figure S7). On the other hand, the rotation of Y241 towards the TM7 in the Apo state resulted in the formation of a different edge connecting TM3 and TM7, and, at the same time, the influence of TM6 in the network is reduced. Finally, the intermediate localization of the Y241 side chain for the Trans system did not allow the connection of TM3 either with TM6 or TM7. This different topology of the network is strictly related to the optimal pathways of propagation of the structural signalling, from the binding site to the G-protein-coupled residues. The pivotal role of Y241 was confirmed by its role in the mediation of W88-H224 and E265-Y106 communications, which were conveyed mainly through TM3 and TM6 (Figure 5). On the other hand, the W88-H224 connection relied almost entirely on TM3 for both Apo and Trans systems, which instead showed different E265-Y106 communication paths. Whereas the Y271-N96 edge allowed a direct connection from TM7 to TM3 in the Apo state, the mediation of TM2 was observed in the Trans state.

Therefore, this study suggests how the “toggle-switch” represented by Y241 side chain rotation could induce TAS2R46 activation without evident conformational changes in the IC region of the receptor. The rotation of Y241 in TM6 towards the centre of the 7TM bundle allows for the formation of an interaction with N92 in TM3, which forms a bridge through which the vibrational information can be transferred between the two helices whose IC regions are involved in G-protein binding. This is also associated with different dynamical behaviour of the receptor, which, in the presence of strychnine, is characterized by higher correlations between the IC and EC regions. In this way, the structural signalling generated by ligand binding is directly transferred to the G-protein binding sites, possibly inducing G-protein activation.

It is worth mentioning that these results are derived from the analysis of the sole TAS2R46, which is the only bitter taste receptor that has been experimentally resolved. Moreover, the receptor structures were embedded into a homogeneous POPC bilayer, despite it is known that the membrane composition can modulate GPCRs function, stability, and signalling (Gimpl, 2016; Sengupta et al., 2018). Therefore, further studies will be needed, considering the possible effects of membrane composition and different TAS2Rs to fully characterize their activation process.

This study represents an important advance toward the comprehension of TAS2R activation mechanisms. Indeed, the improvement of our understanding of these types of machinery could not only shed light on the molecular mechanisms at the basis of the bitter taste perception but can also pave the way towards the rational drug design of compounds able to selectively and specifically trigger their activation. Moreover, considering the expression of TAS2Rs outside the oral cavity and their involvement in several functions beyond the mere taste perception, the obtained molecular insights could be promising results also for engineering compounds targeting specific extra-oral TAS2Rs and modulating their functions.

5 Conclusion

The present study sheds light on the intricate molecular mechanisms and features governing the activation of a G protein-coupled receptor, namely the hTAS2R46 bitter taste receptor. Through a comprehensive approach involving molecular dynamics simulations and network-based analysis, we have unravelled key insights into conformational properties, global intra-structural correlations and structural signalling processes associated with TAS2R active or inactive states. The results highlight that TM3 and TM6 are the main helices involved in structural signalling when the receptor is active, while TM6 reduces its influence when strychnine is absent. Moreover, this study confirms previous evidence regarding the importance of Y241 side-chain localization in the activation process and provides additional insights into the effect of such localization on the structural signalling of the receptor. It is worth mentioning that the residue Y241 is not highly conserved among TAS2Rs, implying that diverse activation mechanisms may exist in other TAS2Rs or with other similar agonists. Hence, the proposed methodology could potentially be expanded to investigate the activation mechanisms of other TAS2Rs, aiming to identify both common and specific features in the activation process, which may vary depending on the receptor's promiscuity or selectivity.

In conclusion, this study has unveiled crucial molecular features and essential structural signalling pathways involved in the activation of hTAS2R46. These findings enhance our comprehension of the intricate activation processes within the bitter taste receptor family and the present approach holds promise for characterizing similar protein targets in future studies. Given the obtained results, further exploration of the activation process of TAS2R46 in the presence of various agonists is warranted to discern whether different agonists trigger similar signal transduction mechanisms. Therefore, this work serves as a pivotal starting point for a profound understanding of the precise mechanisms governing TAS2R activation, paving the way for the rational design of small compounds targeting oral or extra-oral TAS2Rs.

6 Acknowledgements

The present work has been developed as part of the VIRTUOUS project, funded by the European Union's Horizon 2020 research and innovation program under the Marie Sklodowska-Curie-RISE Grant Agreement No. 872181 (https://www.virtuoush2020.com/).

7 Author contributions

Marco Cannariato: Conceptualization; Data curation; Formal analysis; Methodology; Software; Validation; Visualization; Writing - original draft; Writing - review & editing. **Riccardo Fanunza**: Conceptualization; Data curation; Formal analysis; Investigation; Validation; Visualization; Writing - review & editing. **Eric A. Zizzi**: Supervision; Writing - review & editing; **Marcello Miceli**: Supervision; Visualization; Writing - review & editing; **Giacomo Di Benedetto**: Supervision; Writing - review & editing; **Marco Agostino Deriu**: Conceptualization; Data curation; Funding acquisition; Project administration; Resources; Supervision; Validation; Visualization; Writing - review & editing; **Lorenzo Pallante**: Conceptualization; Data curation; Methodology; Software; Supervision; Validation; Visualization; Writing - review & editing.

8 Research Data

All the files necessary to reproduce the simulations and the Python scripts for the analysis are accessible at the website https://github.com/lorenzopallante/TAS2R46.

9 Declaration of interests

The authors declare that no financial interest or conflicts of interest exist.

10 References

Bauer, P., Hess, B., Lindahl, E., 2023. GROMACS 2022.5 Manual. https://doi.org/10.5281/ZENODO.7586765

Behrens, M., Meyerhof, W., 2013. Bitter taste receptor research comes of age: From characterization to modulation of TAS2Rs. Seminars in Cell & Developmental Biology 24, 215–221. https://doi.org/10.1016/j.semcdb.2012.08.006

Berendsen, H.J.C., Postma, J.P.M., Van Gunsteren, W.F., DiNola, A., Haak, J.R., 1984. Molecular dynamics with coupling to an external bath. The Journal of Chemical Physics 81, 3684–3690. https://doi.org/10.1063/1.448118

Born, S., Levit, A., Niv, M.Y., Meyerhof, W., Behrens, M., 2013. The human bitter taste receptor TAS2R10 is tailored to accommodate numerous diverse ligands. Journal of Neuroscience 33, 201–213. https://doi.org/10.1523/JNEUROSCI.3248-12.2013

Brockhoff, A., Behrens, M., Massarotti, A., Appendino, G., Meyerhof, W., 2007. Broad Tuning of the Human Bitter Taste Receptor hTAS2R46 to Various Sesquiterpene Lactones, Clerodane and Labdane Diterpenoids, Strychnine, and Denatonium. J. Agric. Food Chem. 55, 6236–6243. https://doi.org/10.1021/jf070503p

Brockhoff, A., Behrens, M., Niv, M.Y., Meyerhof, W., 2010. Structural requirements of bitter taste receptor activation. Proceedings of the National Academy of Sciences of the United States of America 107, 11110–11115. https://doi.org/10.1073/pnas.0913862107

Cannariato, M., Zizzi, E.A., Pallante, L., Miceli, M., Deriu, M.A., in press. Mechanical Communication within the Microtubule through Network-based Analysis of Tubulin Dynamics. Biomech Model Mechanobiol.

Chandrashekar, J., Mueller, K.L., Hoon, M.A., Adler, E., Feng, L., Guo, W., Zuker, C.S., Ryba, N.J.P., 2000. T2Rs Function as Bitter Taste Receptors. Cell 100, 703–711. https://doi.org/10.1016/S0092-8674(00)80706-0

Dalton, J.A., Lans, I., Giraldo, J., 2015. Quantifying conformational changes in GPCRs: glimpse of a common functional mechanism. BMC Bioinformatics 16, 124. https://doi.org/10.1186/s12859-015-0567-3

Di Pizio, A., Levit, A., Slutzki, M., Behrens, M., Karaman, R., Niv, M.Y., 2016. Comparing Class A GPCRs to bitter taste receptors, in: Methods in Cell Biology. Elsevier, pp. 401–427. https://doi.org/10.1016/bs.mcb.2015.10.005

Dickson, C.J., Walker, R.C., Gould, I.R., 2022. Lipid21: Complex Lipid Membrane Simulations with AMBER. J. Chem. Theory Comput. 18, 1726–1736. https://doi.org/10.1021/acs.jctc.1c01217

Dotson, C.D., Zhang, L., Xu, H., Shin, Y.-K., Vigues, S., Ott, S.H., Elson, A.E.T., Choi, H.J., Shaw, H., Egan, J.M., Mitchell, B.D., Li, X., Steinle, N.I., Munger, S.D., 2008. Bitter Taste Receptors Influence Glucose Homeostasis. PLoS ONE 3, e3974. https://doi.org/10.1371/journal.pone.0003974

Fanelli, F., Felline, A., Raimondi, F., Seeber, M., 2016. Structure network analysis to gain insights into GPCR function. Biochemical Society Transactions 44, 613–618. https://doi.org/10.1042/BST20150283

Feng, S., Park, S., Choi, Y.K., Im, W., 2023. CHARMM-GUI *Membrane Builder* : Past, Current, and Future Developments and Applications. J. Chem. Theory Comput. 19, 2161–2185. https://doi.org/10.1021/acs.jctc.2c01246

Gimpl, G., 2016. Interaction of G protein coupled receptors and cholesterol. Chemistry and Physics of Lipids 199, 61–73. https://doi.org/10.1016/j.chemphyslip.2016.04.006

Heinig, M., Frishman, D., 2004. STRIDE: a web server for secondary structure assignment from known atomic coordinates of proteins. Nucleic Acids Research 32, W500–W502. https://doi.org/10.1093/nar/gkh429

Hénin, J., Maigret, B., Tarek, M., Escrieut, C., Fourmy, D., Chipot, C., 2006. Probing a Model of a GPCR/Ligand Complex in an Explicit Membrane Environment: The Human Cholecystokinin-1 Receptor. Biophysical Journal 90, 1232–1240. https://doi.org/10.1529/biophysj.105.070599

Hess, B., Bekker, H., Berendsen, H.J.C., Fraaije, J.G.E.M., 1997. LINCS: A linear constraint solver for molecular simulations. Journal of Computational Chemistry 18, 1463–1472. https://doi.org/10.1002/(SICI)1096-987X(199709)18:12<1463::AID-JCC4>3.0.CO;2-H

Humphrey, W., Dalke, A., Schulten, K., 1996. VMD: Visual molecular dynamics. Journal of Molecular Graphics 14, 33–38. https://doi.org/10.1016/0263-7855(96)00018-5

Hunter, J.D., 2007. Matplotlib: A 2D Graphics Environment. Comput. Sci. Eng. 9, 90–95. https://doi.org/10.1109/MCSE.2007.55

Janaszewska, A., Klajnert-Maculewicz, B., Marcinkowska, M., Duchnowicz, P., Appelhans, D., Grasso, G., Deriu, M.A., Danani, A., Cangiotti, M., Ottaviani, M.F., 2018. Multivalent interacting glycodendrimer to prevent amyloid-peptide fibril formation induced by Cu(II): A multidisciplinary approach. Nano Res. 11, 1204–1226. https://doi.org/10.1007/s12274-017-1734-9

Jensen, A.A., Gharagozloo, P., Birdsall, N.J.M., Zlotos, D.P., 2006. Pharmacological characterisation of strychnine and brucine analogues at glycine and α7 nicotinic acetylcholine receptors. European Journal of Pharmacology 539, 27–33. https://doi.org/10.1016/j.ejphar.2006.04.010

Jumper, J., Evans, R., Pritzel, A., Green, T., Figurnov, M., Ronneberger, O., Tunyasuvunakool, K., Bates, R., Žídek, A., Potapenko, A., Bridgland, A., Meyer, C., Kohl, S.A.A., Ballard, A.J., Cowie, A., Romera-Paredes, B., Nikolov, S., Jain, R., Adler, J., Back, T., Petersen, S., Reiman, D., Clancy, E., Zielinski, M., Steinegger, M., Pacholska, M., Berghammer, T., Bodenstein, S., Silver, D., Vinyals, O., Senior, A.W., Kavukcuoglu, K., Kohli, P., Hassabis, D., 2021. Highly accurate protein structure prediction with AlphaFold. Nature 596, 583–589. https://doi.org/10.1038/s41586-021-03819-2

Kraskov, A., Stögbauer, H., Grassberger, P., 2004. Estimating mutual information. Phys. Rev. E 69, 066138. https://doi.org/10.1103/PhysRevE.69.066138

Lange, O.F., Grubmüller, H., 2005. Generalized correlation for biomolecular dynamics. Proteins 62, 1053–1061. https://doi.org/10.1002/prot.20784

Laurent, B., Chavent, M., Cragnolini, T., Dahl, A.C.E., Pasquali, S., Derreumaux, P., Sansom, M.S.P., Baaden, M., 2015. Epock: rapid analysis of protein pocket dynamics. Bioinformatics 31, 1478–1480. https://doi.org/10.1093/bioinformatics/btu822

Lee, J., Hitzenberger, M., Rieger, M., Kern, N.R., Zacharias, M., Im, W., 2020. CHARMM-GUI supports the Amber force fields. The Journal of Chemical Physics 153, 035103. https://doi.org/10.1063/5.0012280

Lee, S.-J., Depoortere, I., Hatt, H., 2019. Therapeutic potential of ectopic olfactory and taste receptors. Nat Rev Drug Discov 18, 116–138. https://doi.org/10.1038/s41573-018-0002-3

Liggett, S.B., 2014. Bitter taste receptors in the wrong place: novel airway smooth muscle targets for treating asthma. Trans Am Clin Climatol Assoc 125, 64–74; discussion 74-75.

Malavolta, M., Pallante, L., Mavkov, B., Stojceski, F., Grasso, G., Korfiati, A., Mavroudi, S., Kalogeras, A., Alexakos, C., Martos, V., Amoroso, D., Di Benedetto, G., Piga, D., Theofilatos, K., Deriu, M.A., 2022. A survey on computational taste predictors. Eur Food Res Technol 248, 2215–2235. https://doi.org/10.1007/s00217-022-04044-5

Manrique, P.D., Chakraborty, S., Henderson, R., Edwards, R.J., Mansbach, R., Nguyen, K., Stalls, V., Saunders, C., Mansouri, K., Acharya, P., Korber, B., Gnanakaran, S., 2023. Network analysis uncovers the communication structure of SARS-CoV-2 spike protein identifying sites for immunogen design. iScience 26, 105855. https://doi.org/10.1016/j.isci.2022.105855

Melo, M.C.R., Bernardi, R.C., De La Fuente-Nunez, C., Luthey-Schulten, Z., 2020. Generalized correlation-based dynamical network analysis: a new high-performance approach for identifying allosteric communications in molecular dynamics trajectories. The Journal of Chemical Physics 153, 134104. https://doi.org/10.1063/5.0018980

Miceli, M., Deriu, M.A., Grasso, G., 2022. Toward the design and development of peptidomimetic inhibitors of the Ataxin-1 aggregation pathway. Biophysical Journal 121, 4679–4688. https://doi.org/10.1016/j.bpj.2022.10.021

Molecular Operating Environment (MOE), 2022.02 Chemical Computing Group ULC, 1010 Sherbooke St. West, Suite #910, Montreal, QC, Canada, H3A 2R7, 2023., 2022.

Muscat, S., Pallante, L., Stojceski, F., Danani, A., Grasso, G., Deriu, M.A., 2020. The Impact of Natural Compounds on S-Shaped Aβ42 Fibril: From Molecular Docking to Biophysical Characterization. International Journal of Molecular Sciences 21, 2017. https://doi.org/10.3390/ijms21062017

Pallante, L., Malavolta, M., Grasso, G., Korfiati, A., Mavroudi, S., Mavkov, B., Kalogeras, A., Alexakos, C., Martos, V., Amoroso, D., di Benedetto, G., Piga, D., Theofilatos, K., Deriu, M.A., 2021. On the human taste perception: Molecular-level understanding empowered by computational methods. Trends in Food Science & Technology 116, 445–459. https://doi.org/10.1016/j.tifs.2021.07.013

Pallante, L., Rocca, A., Klejborowska, G., Huczynski, A., Grasso, G., Tuszynski, J.A., Deriu, M.A., 2020. In silico Investigations of the Mode of Action of Novel Colchicine Derivatives Targeting β-Tubulin Isotypes: A Search for a Selective and Specific β-III Tubulin Ligand. Frontiers in Chemistry 8. https://doi.org/10.3389/fchem.2020.00108

Pallante Lorenzo, Cannariato Marco, Vezzulli Fosca, Malavolta Marta, Lambri Milena, Deriu Marco A., 2023. Machine Learning Aided Molecular Modelling of Taste to Identify Food Fingerprints. Chemical Engineering Transactions 102, 283–288. https://doi.org/10.3303/CET23102048

Pan, S., Sharma, P., Shah, S.D., Deshpande, D.A., 2017. Bitter taste receptor agonists alter mitochondrial function and induce autophagy in airway smooth muscle cells. American Journal of Physiology-Lung Cellular and Molecular Physiology 313, L154–L165. https://doi.org/10.1152/ajplung.00106.2017

Pándy-Szekeres, G., Caroli, J., Mamyrbekov, A., Kermani, A.A., Keserű, G.M., Kooistra, A.J., Gloriam, D.E., 2023. GPCRdb in 2023: state-specific structure models using AlphaFold2 and new ligand resources. Nucleic Acids Research 51, D395–D402. https://doi.org/10.1093/nar/gkac1013

Roper, S.D., 2017. Taste: Mammalian Taste Bud Physiology ☆, in: Reference Module in Neuroscience and Biobehavioral Psychology. Elsevier, p. B9780128093245029084. https://doi.org/10.1016/B978-0-12-809324-5.02908-4

Salentin, S., Schreiber, S., Haupt, V.J., Adasme, M.F., Schroeder, M., 2015. PLIP: fully automated protein–ligand interaction profiler. Nucleic Acids Res 43, W443–W447. https://doi.org/10.1093/nar/gkv315

Scheer, A., Cotecchia, S., 1997. Minireview: Constitutively Active G Protein-Coupled Receptors: Potential Mechanisms of Receptor Activation. Journal of Receptors and Signal Transduction 17, 57–73. https://doi.org/10.3109/10799899709036594

Sengupta, D., Prasanna, X., Mohole, M., Chattopadhyay, A., 2018. Exploring GPCR–Lipid Interactions by Molecular Dynamics Simulations: Excitements, Challenges, and the Way Forward. J. Phys. Chem. B 122, 5727–5737. https://doi.org/10.1021/acs.jpcb.8b01657

Soncini, M., Vesentini, S., Ruffoni, D., Orsi, M., Deriu, M.A., Redaelli, A., 2007. Mechanical response and conformational changes of alpha-actinin domains during unfolding: a molecular dynamics study. Biomech Model Mechanobiol 6, 399–407. https://doi.org/10.1007/s10237-006-0060-z

Sullivan, H.-J., Tursi, A., Moore, K., Campbell, A., Floyd, C., Wu, C., 2020. Binding Interactions of Ergotamine and Dihydroergotamine to 5-Hydroxytryptamine Receptor 1B (5-HT $_{1b}$) Using Molecular Dynamics Simulations and Dynamic Network Analysis. J. Chem. Inf. Model. 60, 1749–1765. https://doi.org/10.1021/acs.jcim.9b01082

Sztandera, K., Gorzkiewicz, M., Dias Martins, A.S., Pallante, L., Zizzi, E.A., Miceli, M., Bątal, M., Reis, C.P., Deriu, M.A., Klajnert-Maculewicz, B., 2021. Noncovalent Interactions with PAMAM and PPI Dendrimers Promote the Cellular Uptake and Photodynamic Activity of Rose Bengal: The Role of the Dendrimer Structure. Journal of Medicinal Chemistry acs.jmedchem.1c01080. https://doi.org/10.1021/acs.jmedchem.1c01080

Tian, C., Kasavajhala, K., Belfon, K.A.A., Raguette, L., Huang, H., Migues, A.N., Bickel, J., Wang, Y., Pincay, J., Wu, Q., Simmerling, C., 2020. ff19SB: Amino-Acid-Specific Protein Backbone Parameters Trained against Quantum Mechanics Energy Surfaces in Solution. J. Chem. Theory Comput. 16, 528–552. https://doi.org/10.1021/acs.jctc.9b00591

Topin, J., Bouysset, C., Pacalon, J., Kim, Y., Rhyu, M., Fiorucci, S., Golebiowski, J., 2021. Functional molecular switches of mammalian G protein-coupled bitter-taste receptors. Cellular and Molecular Life Sciences 6, 2020.10.23.348706. https://doi.org/10.1007/s00018-021-03968-7

Wang, J., Wolf, R.M., Caldwell, J.W., Kollman, P.A., Case, D.A., 2004. Development and testing of a general amber force field. J. Comput. Chem. 25, 1157–1174. https://doi.org/10.1002/jcc.20035

Waskom, M., 2021. seaborn: statistical data visualization. JOSS 6, 3021. https://doi.org/10.21105/joss.03021

Xu, W., Wu, L., Liu, S., Liu, X., Cao, X., Zhou, C., Zhang, J., Fu, Y., Guo, Y., Wu, Y., Tan, Q., Wang, L., Liu, J., Jiang, L., Fan, Z., Pei, Y., Yu, J., Cheng, J., Zhao, S., Hao, X., Liu, Z.-J., Hua, T., 2022. Structural basis for strychnine activation of human bitter taste receptor TAS2R46. Science 377, 1298–1304. https://doi.org/10.1126/science.abo1633

Zhang, Haonan, Qiao, A., Yang, D., Yang, L., Dai, A., De Graaf, C., Reedtz-Runge, S., Dharmarajan, V., Zhang, Hui, Han, G.W., Grant, T.D., Sierra, R.G., Weierstall, U., Nelson, G., Liu, W., Wu, Y., Ma, L., Cai, X., Lin, G., Wu, X., Geng, Z., Dong, Y., Song, G., Griffin, P.R., Lau, J., Cherezov, V., Yang, H., Hanson, M.A., Stevens, R.C., Zhao, Q., Jiang, H., Wang, M.-W., Wu, B., 2017. Structure of the full-length glucagon class B G-protein-coupled receptor. Nature 546, 259–264. https://doi.org/10.1038/nature22363

Zhou, Q., Yang, D., Wu, M., Guo, Y., Guo, W., Zhong, L., Cai, X., Dai, A., Jang, W., Shakhnovich, E.I., Liu, Z.-J., Stevens, R.C., Lambert, N.A., Babu, M.M., Wang, M.-W., Zhao, S., 2019. Common activation mechanism of class A GPCRs. eLife 8, e50279. https://doi.org/10.7554/eLife.50279

Zizzi, E.A., Cavaglià, M., Tuszynski, J.A., Deriu, M.A., 2022. Alteration of lipid bilayer mechanics by volatile anesthetics: Insights from μs-long molecular dynamics simulations. iScience 25, 103946. https://doi.org/10.1016/j.isci.2022.103946

Zou, Ewalt, Ng, 2019. Recent Insights from Molecular Dynamics Simulations for G Protein-Coupled Receptor Drug Discovery. IJMS 20, 4237. https://doi.org/10.3390/ijms20174237

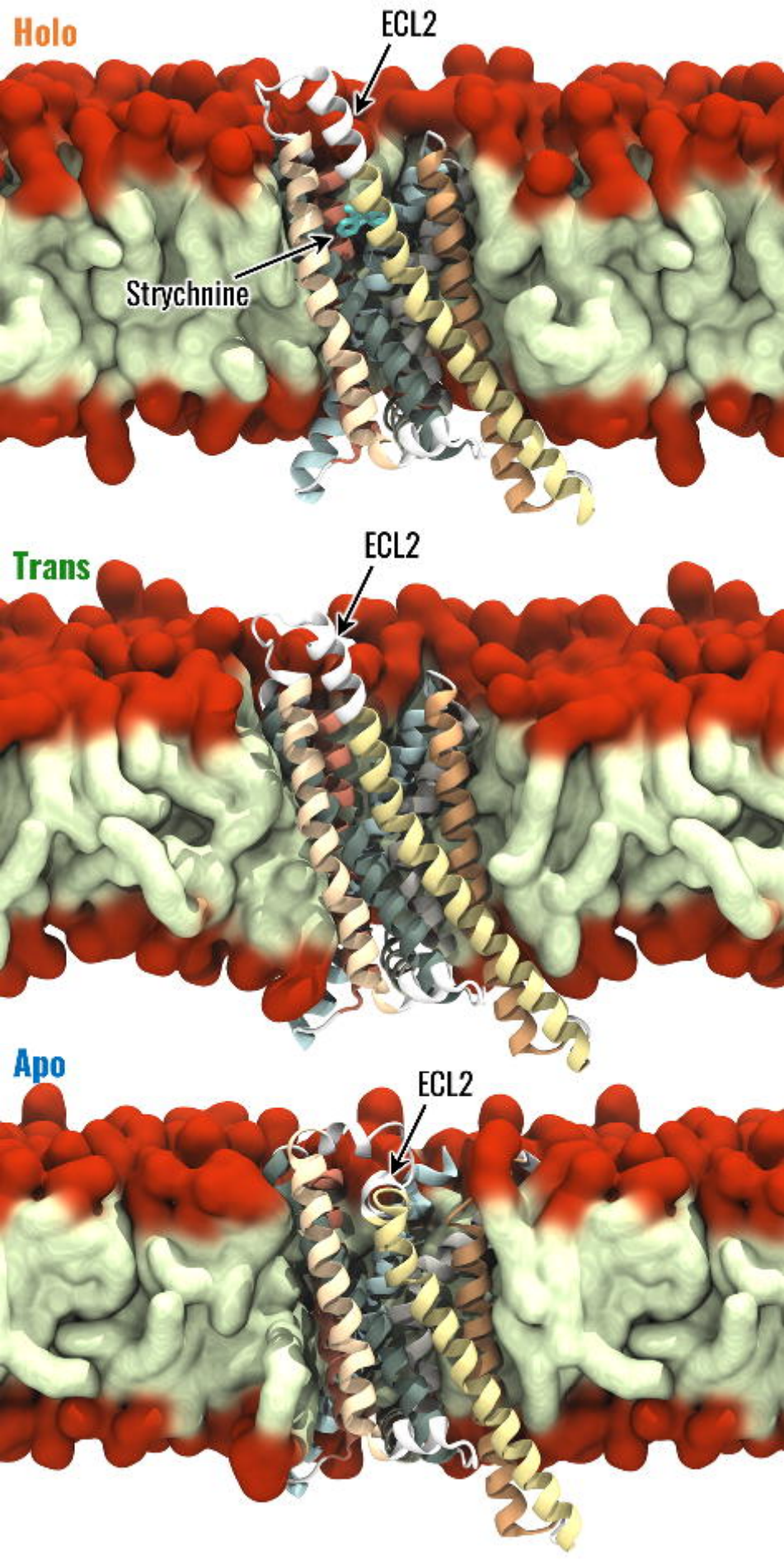
Holo
ECL2
Strychnine
Trans
ECL2
Apo
ECL2

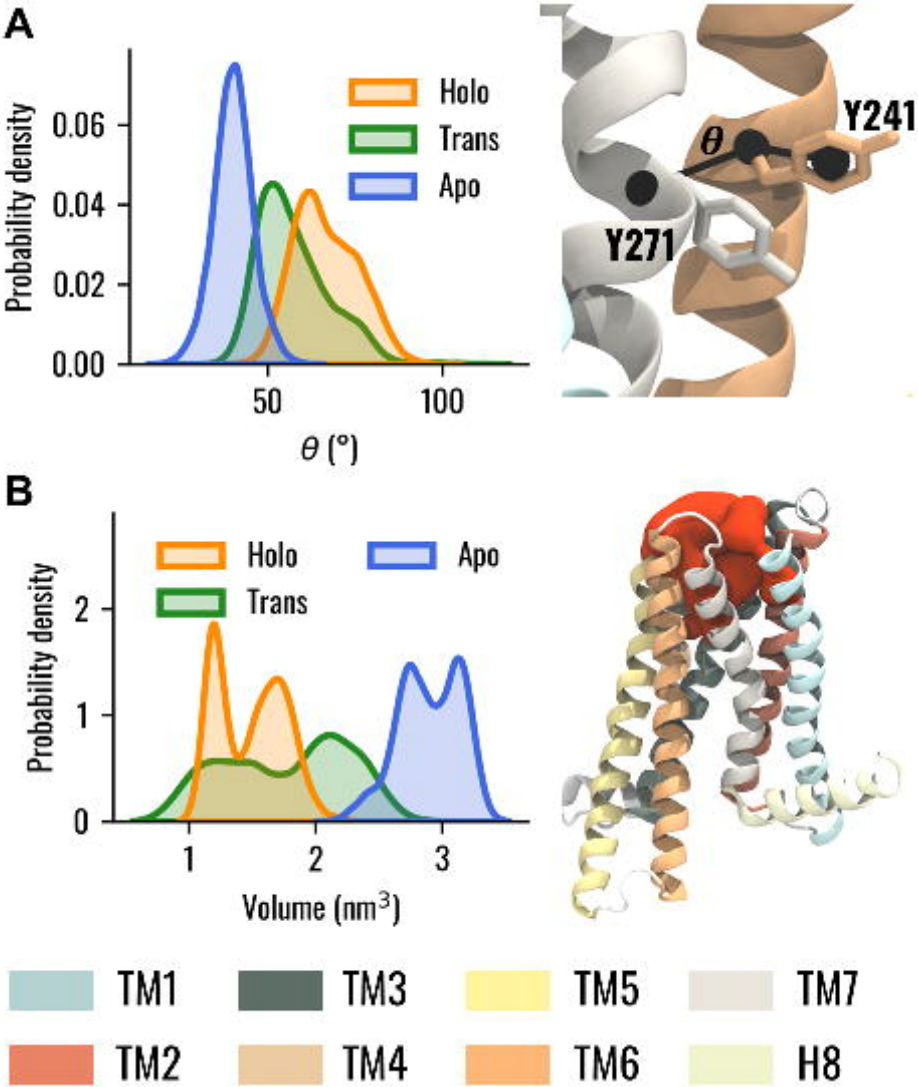
A
Probability density
0.06
0.04
0.02
0.00
50
100
θ (°)
Holo
Trans
Apo
Y241
θ
Y271
B
Probability density
2
1
0
1
2
3
Volume (nm³)
Holo
Trans
Apo
TM1
TM3
TM5
TM7
TM2
TM4
TM6
H8

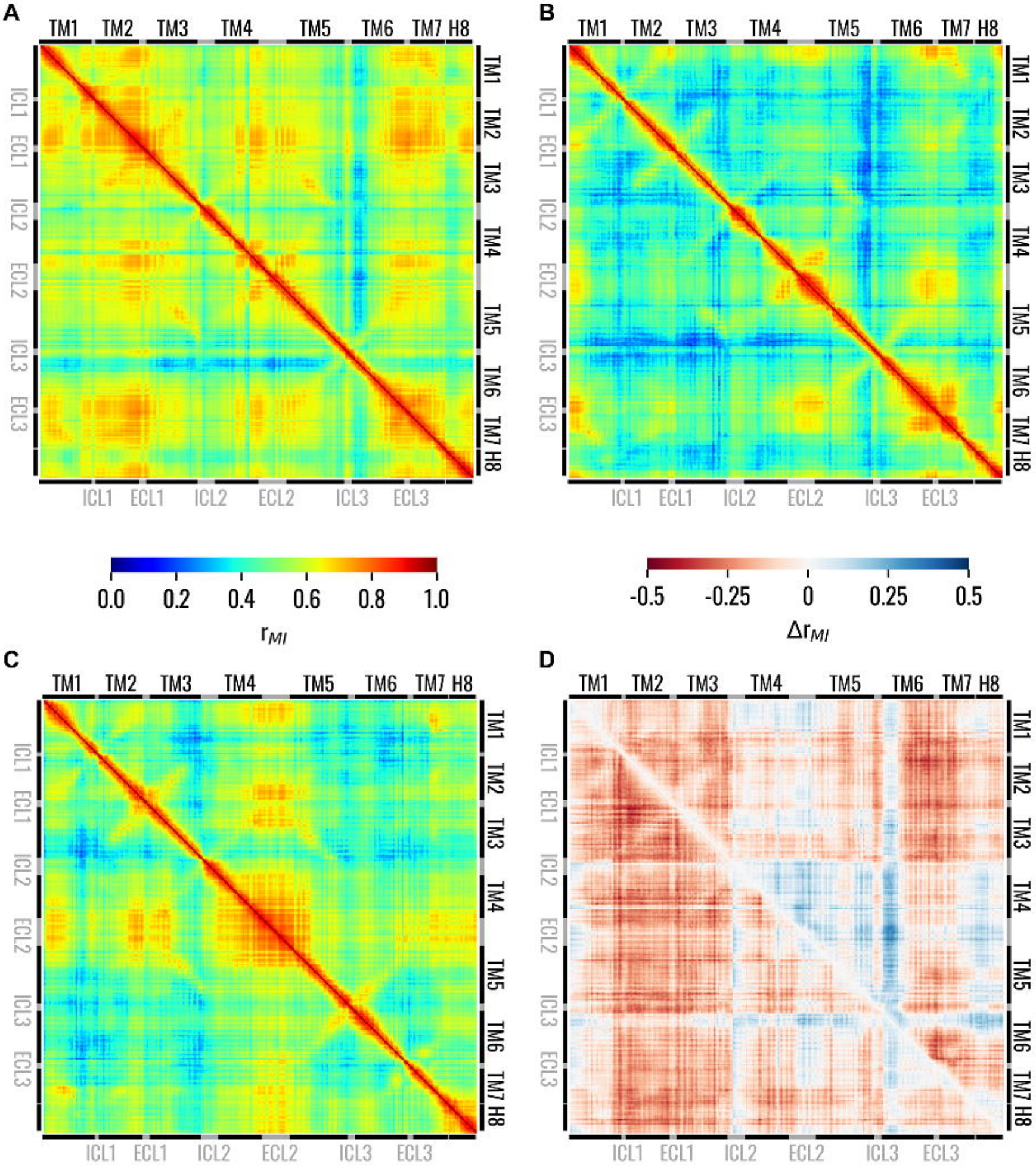
A
B
C
D
TM1
TM2
TM3
TM4
TM5
TM6
TM7
H8
ICL1
ECL1
ICL2
ECL2
ICL3
ECL3
0.0
0.2
0.4
0.6
0.8
1.0
r_{MI}
-0.5
-0.25
0
0.25
0.5
Δr_{MI}

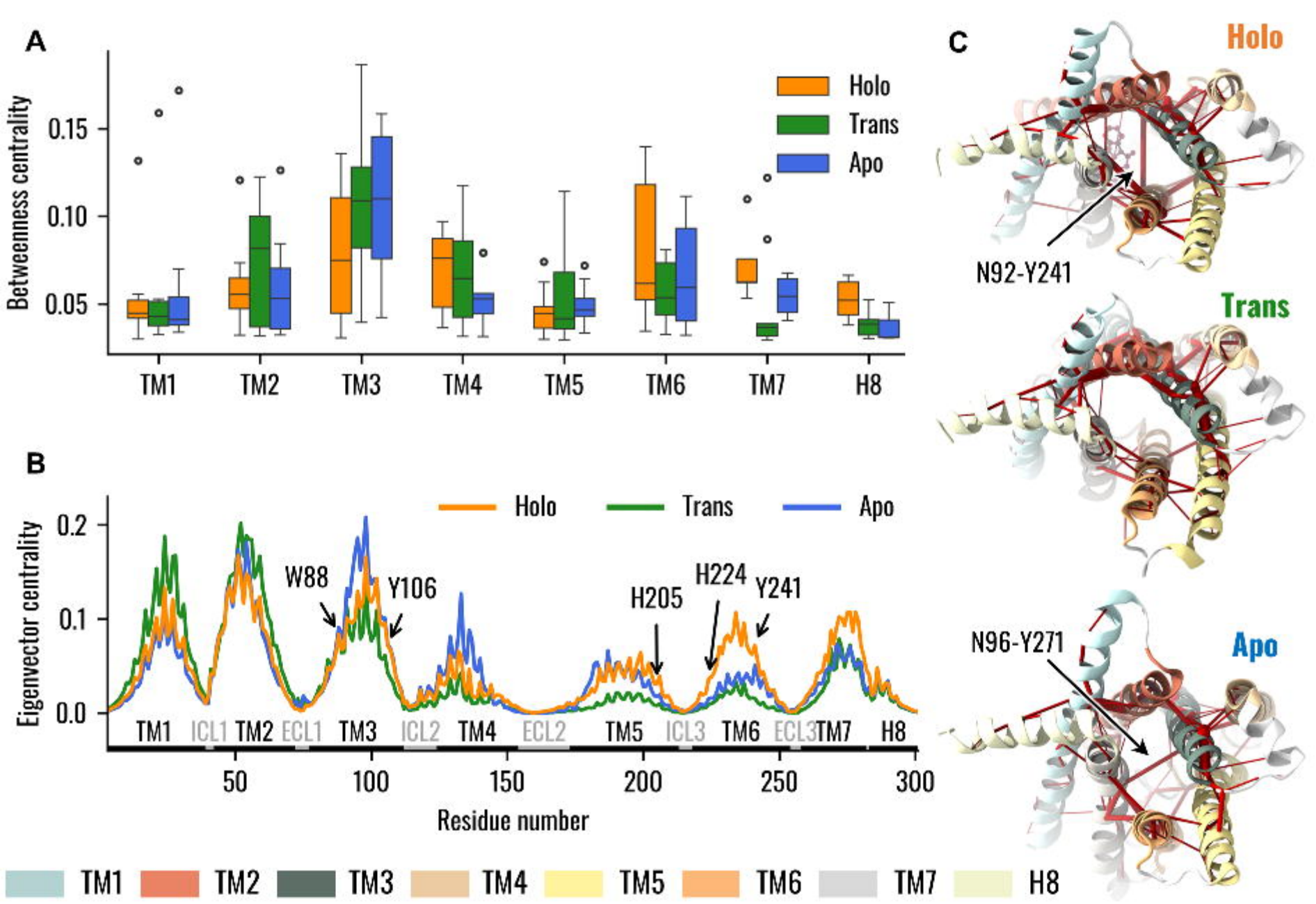
A
Betweenness centrality
0.15
0.10
0.05
Holo
Trans
Apo
TM1
TM2
TM3
TM4
TM5
TM6
TM7
H8
B
Eigenvector centrality
0.2
0.1
0.0
Holo
Trans
Apo
W88
Y106
H205
H224
Y241
TM1
ICL1
TM2
ECL1
TM3
ICL2
TM4
ECL2
TM5
ICL3
TM6
ECL3
TM7
H8
50
100
150
200
250
300
Residue number
C
Holo
N92-Y241
Trans
N96-Y271
Apo
TM1
TM2
TM3
TM4
TM5
TM6
TM7
H8

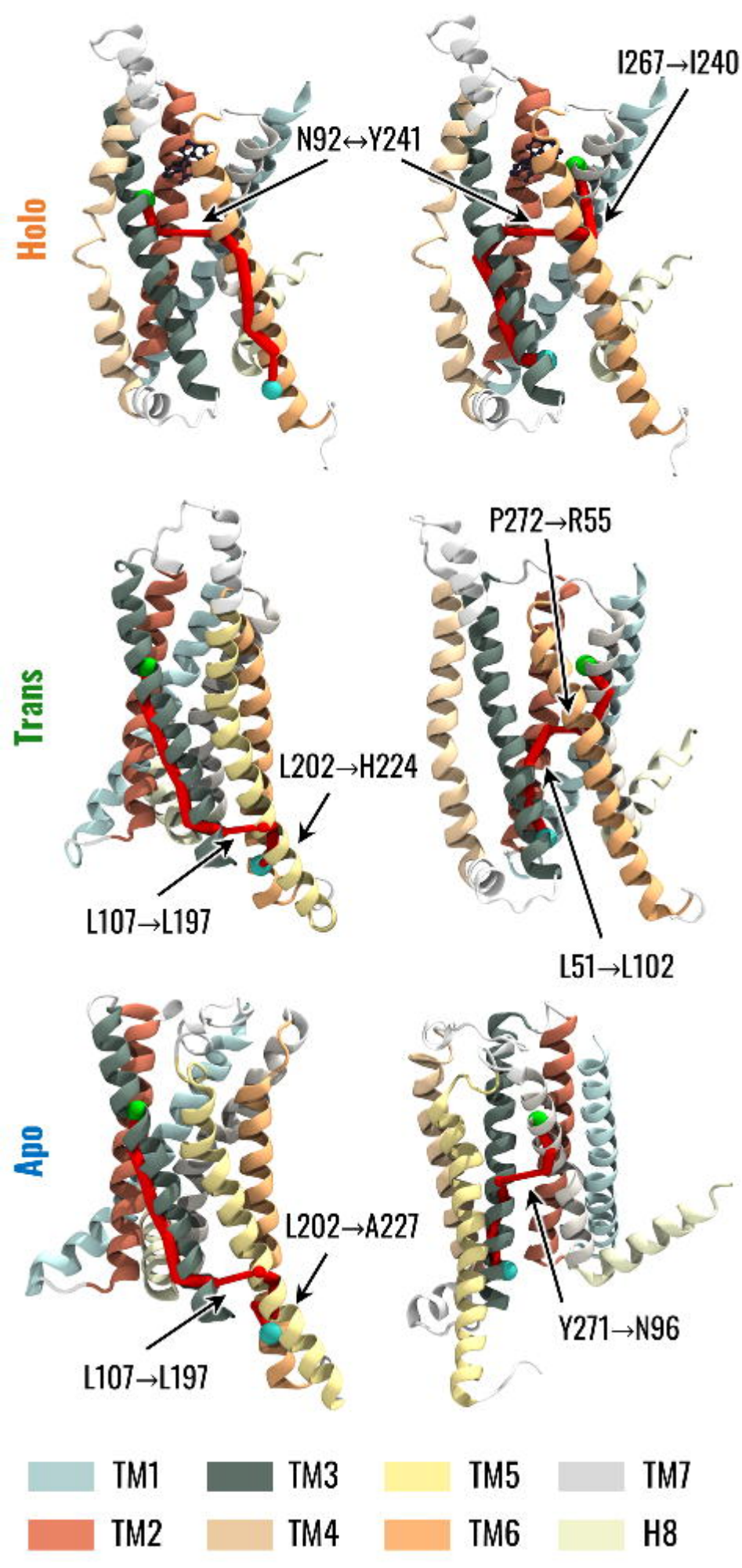
Holo
N92↔Y241
I267→I240
Trans
L202→H224
L107→L197
P272→R55
L51→L102
Apo
L202→A227
L107→L197
Y271→N96
TM1
TM3
TM5
TM7
TM2
TM4
TM6
H8